Proceedings of the Seventh International Conference on
Railway Technology: Research, Development and Maintenance
Edited by: J. Pombo
Civil-Comp Conferences, Volume 15, Paper 6.11
Civil-Comp Press, Edinburgh, United Kingdom, 2026
ISSN: 2753-3239, doi: 10.4203/ccc.15.6.11

Validation of Synthetic Tailored Crossing Frog Geometries by Means of Multibody Simulation

S. Antia-Vallecillo[1], A. Astiazaran[2,1], J. Sagarzazu[2,3], B. Rodríguez-Arana[2,1], J. Nieto[2,1] and N. Gil-Negrete[1]

[1]Tecnun, Universidad de Navarra, Donostia – San Sebastián, Spain
[2]Ceit-Basque Research and Technology Alliance (BRTA), Donostia – San Sebastián, Spain
[3]University of the Basque Country UPV/EHU, Donostia-San Sebastián, Spain

Abstract

Conventional crossing frogs represent a discontinuity in the train passage along rail turnouts, making them prone to impacts. Existing standards and technical referencesgive guidelines for an optimal design of these components. The following paper validates a crossing geometry using Multibody Simulation (MBS), generated keeping in mind maximum speed and traffic type for its design, amongst others. The validation is performed ny means of a reference case of the same geometric characteristics, comparing contact forces and positions.

Keywords: switches and crossings, crossing frog geometry, variable rail, virtual validation, vehicle/track interaction, multibody simulation.

1 Introduction

Rail geometry variations along crossing panels continuously alter wheel-rail contact conditions, increasing dynamic loads and interfacial stress. Crossing frogs are usually mass produced and placed in track for standard traffic conditions and geometries. However, this becomes a problem when these conditions do not fulfill, leading to a non-optimal performance. This accelerates wear, plastic deformation, and rolling contact fatigue [1]. Given the severe time constraints and high financial costs associated with experimental testing, the sector has increasingly pivoted towards numerical solutions.

As a result, Multibody System (MBS) simulation has become the preeminent numerical strategy for analysing the complex dynamics of both vehicle-track and vehicle-turnout interactions. To function correctly, these computational models strictly require precise definitions of wheel and rail geometries. Contact algorithms within MBS frameworks typically rely on elastic half-space theories, which inherently bypass material plasticity considerations [2]. Furthermore, to streamline processing, a co-running track methodology is standard practice. This approach features a simplified track representation, characterized by a reduced set of degrees of freedom (DOFs) to account for vital infrastructure like sleepers and rails, that travels concurrently under the wheelset at an identical speed to the vehicle.

The accuracy of these simulation tools was extensively tested in a 2021 benchmark study focusing on railway MBS dynamics for switches and crossings (S&C) [3]. By employing the Manchester Benchmark passenger vehicle, researchers evaluated two distinct S&C layouts, using discrete transversal cross-sections to define the track geometry. The benchmark verified that existing software reliably captures kinematics and dynamic forces [4].

Additionally, previous studies have addressed crossing frog geometry and its effect on performance. [5] studied longitudinal rail transitions on crossing panels. [6],[7] changed crossing nose shape parameters by using as optimization variables wear number and maximum pressure. [8] optimized both wing rail and nose cross-profiles using worn wheels as a source for the algorithms. Lastly, [9] evaluated turnout layout designs for optimizing performance.

Therefore, there is a need to generate geometries tailored for the traffic ingoing. Also, the geometries need to be validated before extending the methodology to different scenarios. The following document explains the geometrical design of a crossing nose component from scratch and makes a dynamic comparison to a reference case.

2 Methods

This section describes the main geometrical characteristics required to generate a synthetic crossing, along with the simulation procedure used for validation.

2.1 Geometry

A crossing frog is composed of two main parts: the wing rail and the nose. On the one hand, the wing rail covers from the constant Vignole rail to the crossing nose transition, extended as well in parallel to the nose for impeding the wheel to derail. On the other hand, the crossing nose covers from the transition to the exiting Vignole rail. Their positioning and shape play a key role on the load transference process when approaching the nose.

2.1.1 Wing rail

The wing rail profile base is a standard Vignole rail, 60E1 for example. This profile may have an inclination with respect to the vertical reference. As the wing rail has to support higher loads than the standard rail, the shape is modified to adapt to the wheel shape (normally considering a common worn wheel). Therefore, the profile ends with a slope according to the criteria presented, as seen in Figure 1.

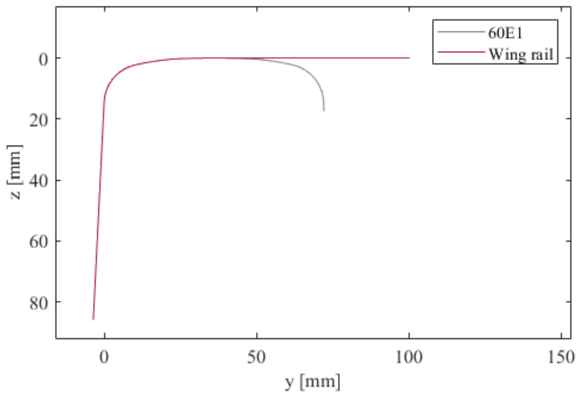

Figure 1. Wing rail cross-profile.

Regarding the wing rail layout, the orientation diverts from the running one in an outwards direction from the throat opening, which takes a higher value than the flangeway width. This is done because the wheel flange may impact with the opposite wing rail if it is too straight. However, if the wing rail is placed too far from the running trajectory, it may cause high contact stresses on the load transference from the wing rail to the nose. Baluch's theory gives a maximal value for this deviation angle θ presented in Figure 2, according to the maximum speed allowed for the turnout V_{max}:

$$tg(\theta) = \frac{\sqrt{W_0}}{V_{max}}$$

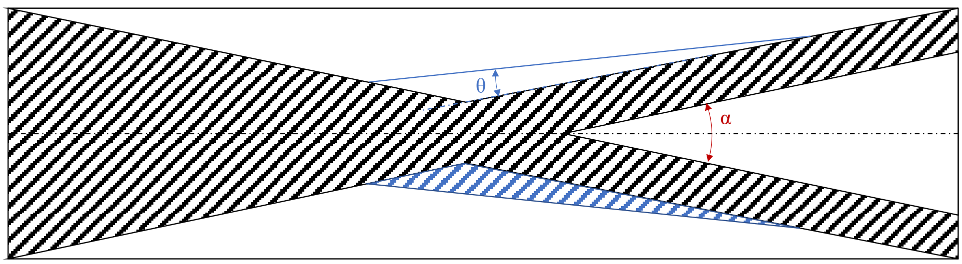

Figure 2. Baluch's theory. α: crossing vee angle, θ: Baluch's angle.

Where $W_0 = 6\ {km^2}/{h^2}$ for most cases [10]. A deviation is also applied to the vee of the frog, to further improve the performance when taking the frog in the opposite direction. As at the vee the axes are not impeded by the respecting check rail, added to the fact that turnouts have a width increase on the deviated direction, the opening angle also takes a higher value according to the angle of attack and the width increase.

2.1.2 Nose

The nose profile, for its part, has a 1:4 slope inwards the running edge, contrary to the wing rail which ends with a 1:20 slope, see Figure 3. This ensures a proper contact with the wheel tread.

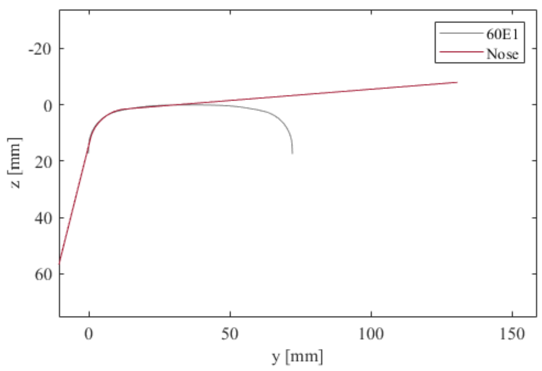

Figure 3. Nose cross-profile.

The load transference from the wing rail to the nose will depend on the height positioning of the profiles used. Thus, normally one of two measures (or both) are taken. On the one hand, the wing rail can be elevated with respect to the running band. On the other hand, the nose can be lowered on the most critical zone. For this case, just the second alternative is applied, as shown in Figure 4.

As the crossing vee is composed of an intersection of profiles, the width will depend on the position away from the MNP (Mathematical Nose Point, x=0) [11]. This width will determine how much is the nose profile lowered, and depends on the ingoing traffic and the geometry of the wing rail profile [12]. Just the running band is lowered, keeping the rest of the profile in place.

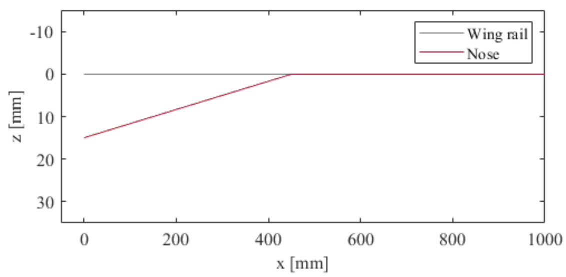

Figure 4. Nose longitudinal profile.

Another design characteristic is the retraction of the point away from the MNP. This increases the clearance for the wheel flange to avoid potential impacts. The point is machined as well, giving it a blunt shape with respect to the sharp nose, called the Real Nose Point (RNP).

The nose profile changes as the loads are already transferred and the MNP is left away, turning into the wing rail profile again. This reduces the contact patch avoiding conformal contact. A transition is created from the nose profile to the wing rail profile, and once again from the wing rail to the Vignole rail approaching the exit [13].

2.2 Simulation

To conduct the dynamic simulations within this study, the well-established vehicle model originally defined in the Manchester Benchmark [14] has been adopted. This chosen configuration accurately replicates the mechanical characteristics of a standard passenger railway coach. Structurally, the vehicle is supported by a dual-bogie architecture, wherein each individual bogie incorporates two independent wheelsets, ultimately comprising a complete eight-wheel system. A visual representation of this multibody vehicle model is provided in Figure 5. Additionally, the operational parameters stipulate the implementation of an S1002 wheel profile, configured to interact with a standard track gauge of 1435 mm.

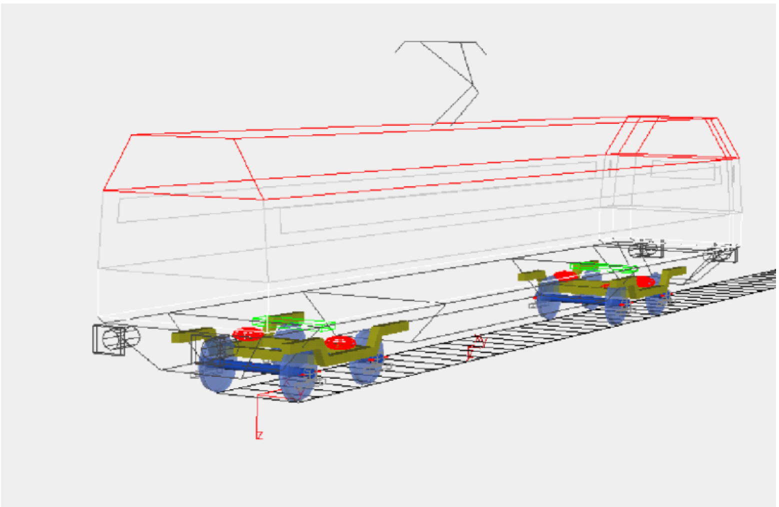

Figure 5. Image of the vehicle model.

This study focuses on scenarios RUN 7 and RUN 8, which evaluate the through and diverging routes of a Swedish 60E1 crossing, respectively. The specific operational parameters governing these simulations are fully detailed in Table 1. As explicitly illustrated in Figure 6, the origin of the longitudinal coordinate system (s = 0 m) is established exactly at the crossing nose point, serving as the absolute reference for the dynamic analysis. Furthermore, in all evaluated cases, the varying track geometry is consistently located on the right-hand side of the track layout.

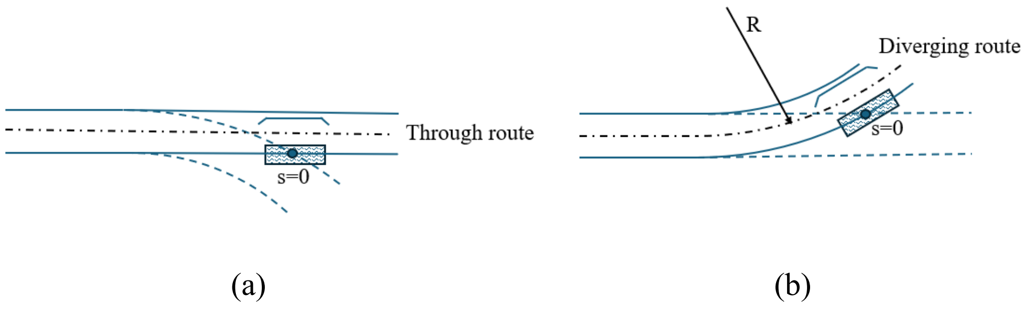

Figure 6. Representation of the trajectories and location of varying geometry. Through route (a) and Diverging route (b).

For these scenarios, the simulations utilize a co-running track methodology. The multibody track model is structured using four discrete bodies: the main track block and three individual rails, specifically the left rail, the right rail, and the check rail. Figure 7 illustrates this topological arrangement. In this framework, the vehicle-track interaction generates three distinct contact-pairs. The left wheel undergoes simultaneous contact with both the left rail and the check rail, while the right wheel establishes a single contact with the right rail. Additionally, variable cross-sectional geometry is introduced along the longitudinal axis for both the right rail and the check rail to represent the track layout changes. The structural parameters governing these connections are detailed in Table 2.

Table 1. Description of routes and velocities.

Scenario	Rail	Route	Velocity (km/h)	Radius (m)
7	60E1	Through	160	-
8	60E1	Diverging	80	760

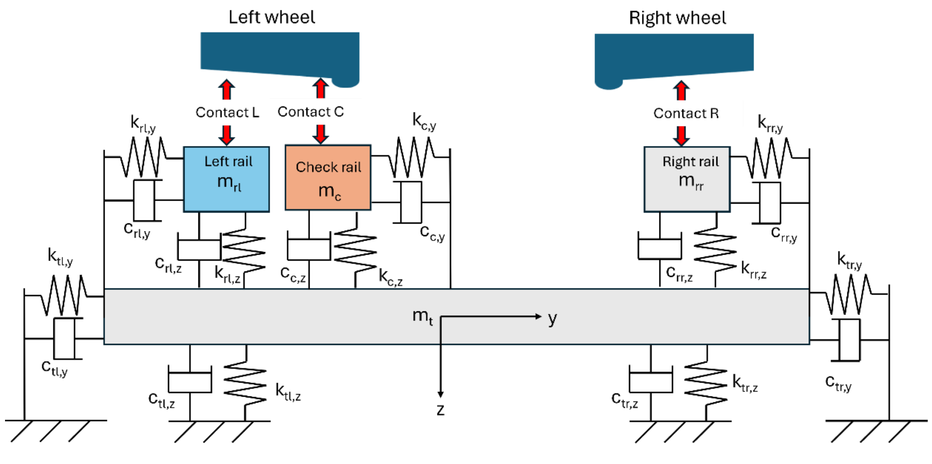

Figure 7. Topology of the track.

Table 2. Track parameters for independent bodies approach [3] and equivalent body approach.

Parameter		Values
Masses (kg)		
Track mass	m_t	2000
Left rail mass	m_{rl}	60
Check rail mass	m_c	60
Right rail mass	m_{rr}	180
Stiffness (kN/m)		
Lateral left rail-sleeper	$k_{rl,y}$	30000
Vertical left rail-sleeper	$k_{rl,z}$	150000
Lateral check rail-sleeper	$k_{c,y}$	30000
Vertical check rail-sleeper	$k_{c,z}$	150000
Lateral right rail-sleeper	$k_{rr,y}$	30000
Vertical right rail-sleeper	$k_{rr,z}$	500000
Lateral left and right sleeper-ballast	$k_{tl,y}/k_{tr,y}$	100000
Vertical left and right sleeper-ballast	$k_{tl,z}/k_{tr,z}$	200000
Damping (kNs/m)		
Lateral left rail-sleeper	$c_{rl,y}$	150
Vertical left rail-sleeper	$c_{rl,z}$	100
Lateral check rail-sleeper	$c_{c,y}$	150
Vertical check rail-sleeper	$c_{c,z}$	100
Lateral right rail-sleeper	$c_{rr,y}$	150
Vertical right rail-sleeper	$c_{rr,z}$	350
Lateral left and right sleeper-ballast	$c_{tl,y}/c_{tr,y}$	500
Vertical left and right sleeper-ballast	$c_{tl,z}/c_{tr,z}$	2000

3 Results

The results derived from the simulations, specifically the most representative ones, are presented herein. All displayed graphs feature two distinct curves: the blue curve represents the benchmark results, while the dark red curve constitutes the results obtained via the synthetic generation of crossing sections executed within the scope of this report. An analysis of these obtained results will follow.

3.1 Geometry

The case study uses a geometry of the following characteristics:

- Crossing vee angle tangent: $tg(\alpha) = {}^{1}/_{15}$
- Maximum speed: 200 km/h.
- 60E1 rail profile.
- Flangeway width: 42 mm (58 mm on entry).
- Nose elevation profile: $z\ (\Delta y) = \frac{1}{tg(\alpha)} - 0.5 \cdot \Delta y$ (z=0 at least)
- Nose retraction: 135 mm.
- Distance to RNP: 200 mm.

The resulting geometry is shown below, on a 3D view in Figure 8 and compared on several planes in Figure 9.

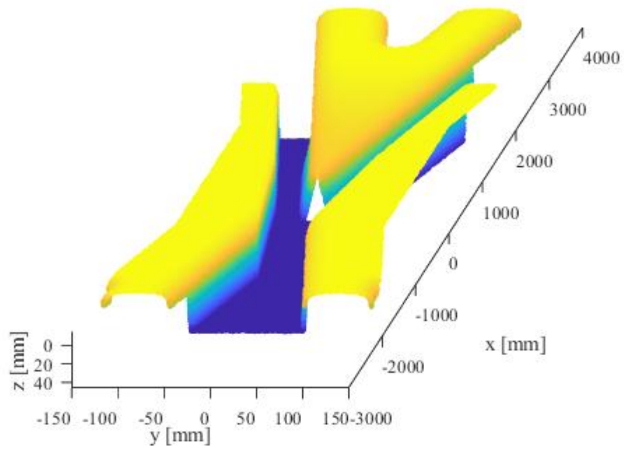

Figure 8. Geometry 3D view.

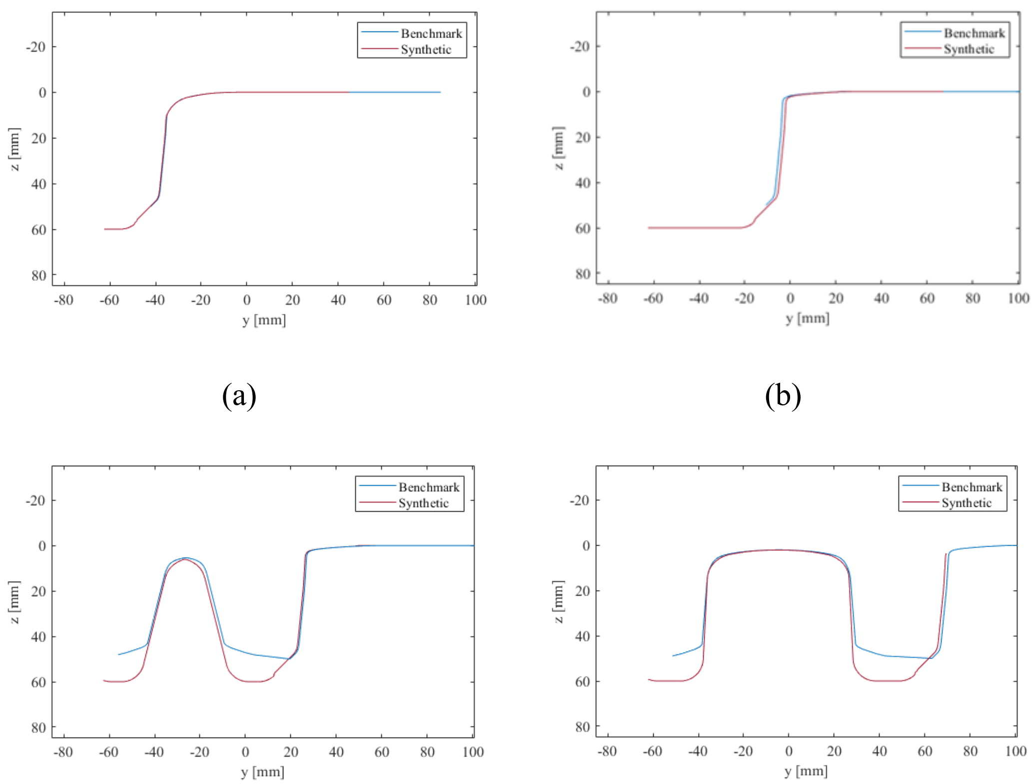

(a) (b)

(c) (d)

Figure 9. Cross-sections on through direction for (a) s=-1000 mm, (b) s=-300 mm, (c) s=300 mm, and (d) s=1000 mm.

3.2 Simulation

The initial phase of analysis addresses vehicle kinematics. Figure 10 presents the lateral displacement of Wheelset 1 (WS1) for both RUN 7 and RUN 8 scenarios. While the overall trajectory morphology is highly consistent between both models across both cases, specific discrepancies are observed in RUN 7. Regarding this scenario, the synthetic model exhibits slightly larger displacement magnitudes immediately following the crossing nose region, with a peak deviation of 0.19 mm recorded at longitudinal position s = 1.5 m. Subsequently, this offset reduces, leading to coinciding peak amplitudes around s = 4 m. During the descent phase, the benchmark trajectory decreases more rapidly, although both signals stabilize towards the end of the analysed track segment.

A similar tendency is observed in the Run 8, where the overall morphology of the lateral displacement curves remains consistent between both models. Following the passage through the crossing nose region, the synthetic trajectory exhibits a higher increase in displacement, culminating in a maximum offset of 0.61 mm relative to the benchmark at longitudinal position s = 2.2 m. Nevertheless, both curves achieve coincident peak magnitudes at the same longitudinal location in s = 3.5 m. In the subsequent stabilization phase following this peak, the benchmark trajectory displays a more oscillatory behaviour, whereas the response from the generated section is notably smoother.

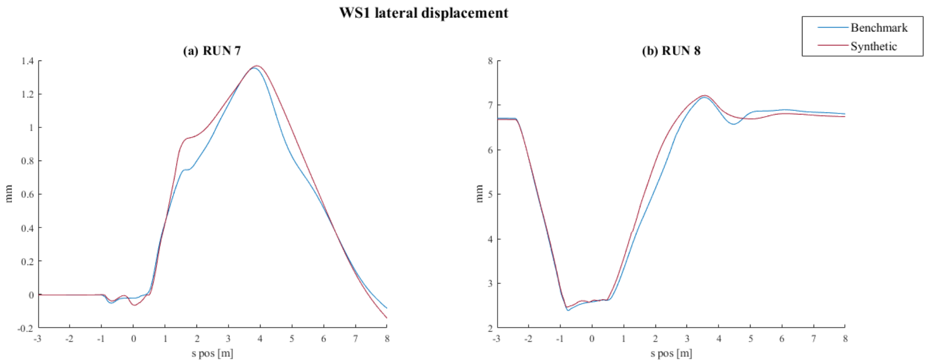

Figure 10. Wheelset 1 lateral displacement: Run 7 (a) and Run 8 (b).

Figure 11 illustrates the evolution of the yaw angle for Wheelset 1 (in mrad) as a function of the longitudinal position along the track. Across both simulation scenarios, the macroscopic morphology of the curves demonstrates a strong correlation between the benchmark and the synthetic signals, although certain localized deviations can be identified upon closer inspection.

In the RUN 7 scenario, the initial positive peak manifests concurrently in both models at a longitudinal position of s = 0.51 m, with the benchmark yielding a marginally lower amplitude. Subsequently, a noticeable phase shift occurs at the second positive peak; the synthetic curve reaches its local maximum approximately 0.5 m earlier than the benchmark, while concurrently exhibiting an amplitude increase of 0.1 mrad. During the subsequent descent into negative yaw values, the absolute minimum occurs at the exact same longitudinal coordinate of s = 4.36 m for both models. However, the synthetic curve registers a less pronounced negative peak, resulting in a magnitude difference of 0.16 mrad when compared to the benchmark trajectory.

Regarding RUN 8, the longitudinal locations of the local maxima and minima are perfectly aligned between the two modelling approaches. Nevertheless, the synthetic model consistently predicts higher absolute values at these extreme points. The most substantial deviation is recorded near s = 1.7 m, where the synthetic signal presents a significant offset of 0.75 mrad relative to the benchmark. Furthermore, the benchmark trajectory features a distinct local maximum at s = 4.7 m, a specific dynamic oscillation that is not replicated by the synthetic model.

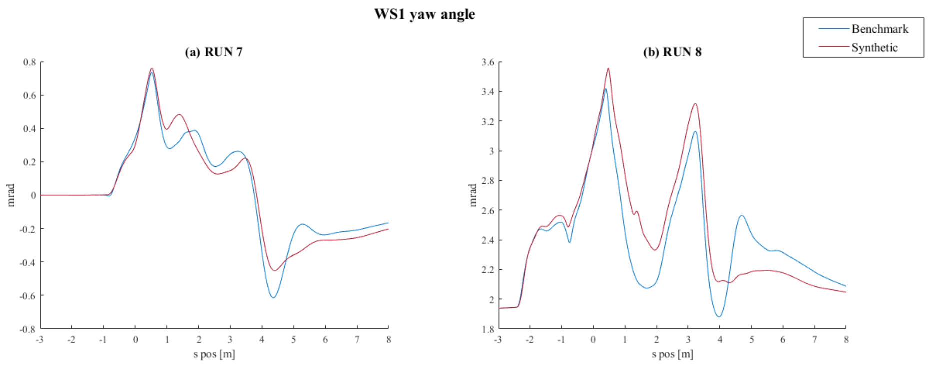

Figure 11. Wheelset 1 yaw angle: Run 7 (a) and Run 8 (b).

Figure 12 illustrates the vertical wheel displacement for both simulation scenarios. The macroscopic profiles of both curves exhibit high similarity, particularly during the ascending phase, which is practically identical across both models. Peak magnitudes are reached at virtually the same longitudinal coordinate, with the benchmark model peaking just 0.1 m prior to the synthetic trajectory.

The primary discrepancies emerge during the descending phase. In RUN 7, the benchmark trajectory features a localized plateau near s = 1.56 m, momentarily sustaining the vertical displacement. The synthetic model does not replicate this stabilization and descends abruptly, resulting in a vertical offset of 0.44 mm. A similar dynamic occurs in RUN 8: the benchmark exhibits a more gradual decrease, whereas the synthetic model shows a steeper, sudden drop. However, as the longitudinal distance increases, this transient deviation fully resolves, and both curves converge to display highly consistent kinematic behaviour.

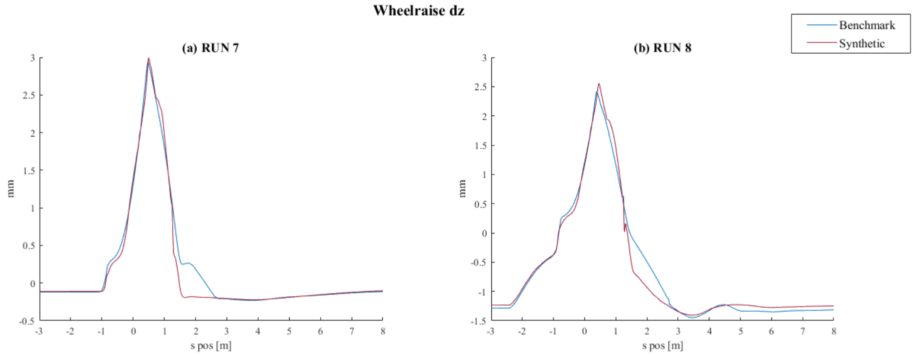

Figure 12. Wheel raise: Run 7 (a) and Run 8 (b).

The subsequent two figures present the dynamic contact forces, specifically illustrating both the vertical and lateral force components generated at the right wheel-rail interface during the simulated scenarios.

Figure 13 presents the right wheel vertical contact forces (Q force R), revealing significant discrepancies between both models compared to the kinematic variables.

In RUN 7, the synthetic response drops to 0 kN at three distinct longitudinal positions (s = - 0.88 m, 0.43 m, and 1.23 m), indicating momentary wheel-rail contact loss entirely absent in the benchmark. The synthetic signal also exhibits substantial high-frequency noise near the crossing nose. While both models reach their maximum peak at approximately the same location, with the benchmark leading by just 0.1 m, the synthetic peak is 23 kN higher and features a prominent secondary maximum not reproduced by the benchmark.

Similarly, in RUN 8, despite initial trajectory alignment, the synthetic curve becomes heavily distorted by noise at the crossing nose. The absolute maximum peak occurs 0.08 m earlier in the benchmark, whereas the synthetic model's apex is 17.5 kN greater. Furthermore, the synthetic model predicts another complete loss of vertical contact at s = 1.28 m, a critical dynamic event that the benchmark simulation does not capture. A peak in vertical forces at s = 2.7 m has not been observed in the results corresponding to the synthetic geometry.

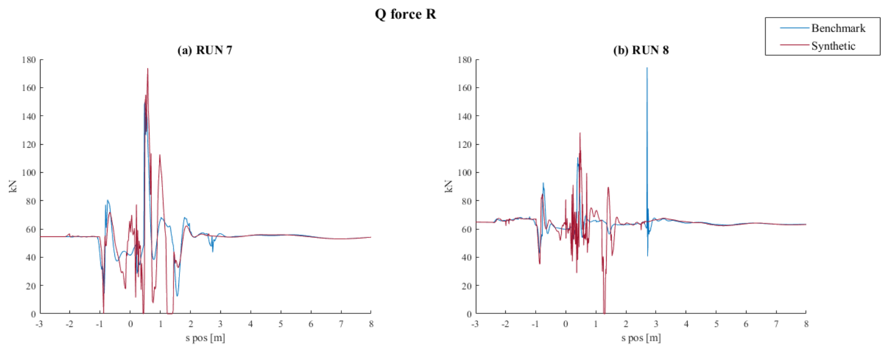

Figure 13. Vertical force: Run 7 (a) and Run 8 (b).

Figure 14 illustrates the lateral contact forces, which exhibit a higher correlation between the models than the vertical forces. However, the synthetic signal still contains significant high-frequency noise, primarily around the crossing nose.

In RUN 7, the two maximum lateral peaks occur simultaneously in both models, but the synthetic magnitudes are greater by 2.8 kN and 2.4 kN, respectively. The synthetic signal also consistently overestimates the absolute values of the local minimum peaks.

In RUN 8, both models behave similarly approaching the crossing nose until substantial noise disrupts the synthetic signal at s = 0.2 m. Following this localized distortion, the two dynamic responses restabilize and remain highly comparable.

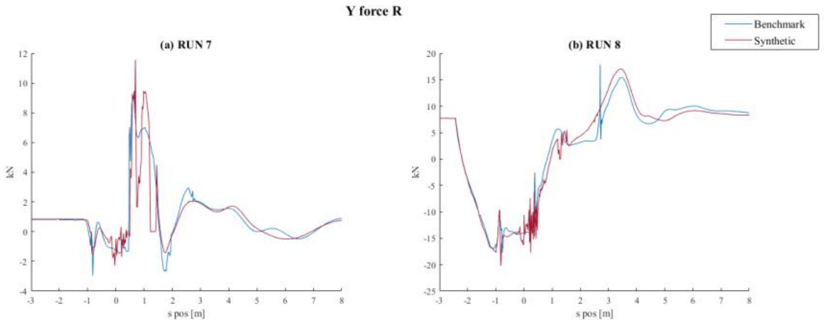

Figure 14. Lateral force: Run 7 (a) and Run 8 (b).

Figure 15 presents the lateral position of the wheel-rail contact points along the longitudinal position. Consistent with modelling definitions, primary contact points are indicated by solid dots, while simultaneous secondary contacts are denoted by open circles of the matching colour. Overall, high qualitative agreement between the benchmark and synthetic signals is observed across both simulation scenarios.

In RUN 7, while the correlation remains strong, a localized discrepancy occurs centred near s = 1.27 m. At this position, the benchmark signal reveals a distinct lateral shift or 'valley' that is not replicated by the synthetic model, which maintains a rectilinear trajectory through this region. In contrast, for RUN 8, this specific lateral shift feature is absent in the benchmark reference, resulting in highly comparable trajectories between the two modelling approaches throughout the segment.

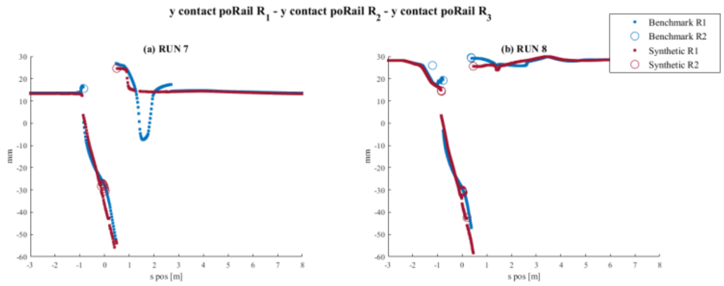

Figure 15. Lateral contact position on rail: Run 7 (a) and Run 8 (b)

Figure 16 presents the right wheel contact force on the check rail. In RUN 7, the straight track alignment requires no lateral guidance, resulting in a constant 0 kN force with no contact. In RUN 8, the wheel actively engages the check rail, and both models exhibit highly similar macroscopic profiles. The initial impact occurs simultaneously at s = - 2.42 m, with the benchmark registering a marginally higher magnitude. As the wheelset negotiates the crossing nose, high-frequency noise slightly distorts the synthetic signal. Finally, during the descent phase, the synthetic trajectory displays an anomalous, isolated peak at s = 1.26 m, which is entirely absent in the benchmark data.

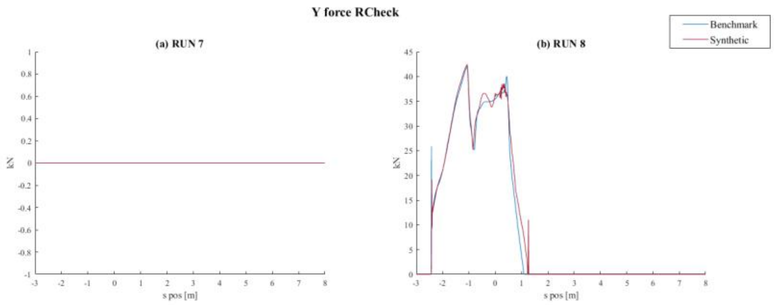

Figure 16. Lateral force on check rail: Run 7 (a) and Run 8 (b)

4 Conclusions & Contributions

The study confirms that reliable synthetic geometries of railway turnout crossing noses can be generated and effectively used in multibody dynamic simulations. These geometries capture the key contact-related features governing wheel–rail interaction and are adjusted to the specific traffic conditions presented. As the low frequency performance has resembled the reference one, the high frequency performance presents noise, which suggests a need for smoothing the geometry amongst others. Some contact losses not present in the reference case are also identified.

Future lines may include simulating real scanned geometries, which will include manufacturing imperfections on the simulation that will have an effect on the dynamic performance of the turnout. Furthermore, obtained multibody signals serve as inputs for deformable solid dynamic simulations as well as for predicting long term evolution of crossing frog geometries.

References

[1] J.C.O. Nielsen, B.A. Pålsson, P.T. Torstensson, Switch panel design based on simulation of accumulated rail damage in a railway turnout, Wear 366–367 (2016) 241–248. https://doi.org/10.1016/j.wear.2016.06.021.
[2] Y. Ma, A.A. Mashal, V.L. Markine, Modelling and experimental validation of dynamic impact in 1:9 railway crossing panel, Tribol. Int. 118 (2018) 208–226. https://doi.org/10.1016/j.triboint.2017.09.036.
[3] Y. Bezin, B.A. Pålsson, Multibody simulation benchmark for dynamic vehicle-track interaction in switches and crossings: modelling description and simulation tasks, Vehicle System Dynamics 61 (2023) 644–659. https://doi.org/10.1080/00423114.2021.1942079.
[4] B.A. Pålsson, Y. Bezin, Editorial for S&C benchmark special issue, Vehicle System Dynamics 61 (2023) 639–643. https://doi.org/10.1080/00423114.2023.2178942.
[5] N. Bosso, A. Bracciali, G. Megna, N. Zampieri, Effects of geometric track irregularities on vehicle dynamic behaviour when running through a turnout, Vehicle System Dynamics 61 (2023) 782–798. https://doi.org/10.1080/00423114.2021.1957127
[6] C. Wan, V.L. Markine, I.Y. Shevtsov, Improvement of vehicle–turnout interaction by optimising the shape of crossing nose, Vehicle System Dynamics 52 (2014) 1517–1540. https://doi.org/10.1080/00423114.2014.944870.
[7] C. Wan, V. Markine, R. Dollevoet, Robust optimisation of railway crossing geometry, Vehicle System Dynamics 54 (2016) 617–637. https://doi.org/10.1080/00423114.2016.1150495.
[8] J. Lee, A. de Arthur, M.S. Dersch, J.R. Edwards, Optimisation of turnout frog profile geometry using revenue service wheel profiles, Vehicle System Dynamics (2023). https://doi.org/10.1080/00423114.2023.2218948.
[9] Y. Cao, E. Kassa, W. Zhao, Evaluation of alternative turnout layout designs for an improved dynamic performance of a vehicle-turnout system, Vehicle System Dynamics 60 (2022) 1722–1741. https://doi.org/10.1080/00423114.2020.1871494.
[10] M.R. Bugarin, J.M. García Díaz de Villegas, Desvíos ferroviarios, Santander : Ingeniería Cántabra, 1995, 1995. https://portalinvestigacion.udc.gal/documentos/608ca839af765575d40a38c6.
[11] B.A. Pålsson, Optimisation of railway crossing geometry considering a representative set of wheel profiles, Vehicle System Dynamics 53 (2015) 274–301. https://doi.org/10.1080/00423114.2014.998242.
[12] NSW RailCorp, ESC 250: TURNOUTS AND SPECIAL TRACKWORK, 2018. www.transport.nsw.gov.au.
[13] EN_13232-6: Railway applications. Track. Switches and crossings for Vignole rails. Part 6: Fixed common and obtuse crossings.
[14] S. Iwnicki, Manchester benchmarks for rail vehicle simulation, Vehicle System Dynamics 30 (1998) 295–313. https://doi.org/10.1080/00423119808969454.